Journal of Materials Chemistry A

Cite this: J. Mater. Chem. A, 2019, 7, 12068

Sulfur-deficient MoS_2 grown inside hollow mesoporous carbon as a functional polysulfide mediator†

Hong-En Wang,*[a] Xuecheng Li,[a] Ning Qin,[c] Xu Zhao,[d] Hua Cheng,[c] Guozhong Cao*[e] and Wenjun Zhang*[b]

Lithium–sulfur (Li–S) batteries are regarded as one of the most promising next-generation electrochemical cells. However, shuttling of lithium polysulfide intermediates and sluggish kinetics in random deposition of lithium sulfide (Li_2S) have significantly degraded their capacity, rate and cycling performance. Herein, few-layered MoS_2 nanosheets enriched with sulfur vacancies are anchored inside hollow mesoporous carbon (MoS_{2-x}/HMC) *via* S–C bonding and proposed as a novel functional mediator for Li–S batteries. Ultrathin MoS_2 sheets with abundant sulfur vacancies have strong chemical affinity to polysulfides and in the meantime catalyze their fast redox conversion with enhanced reaction kinetics as proved by experimental observations and first-principles density functional theory (DFT) calculations. At a current density of 1C, the MoS_{2-x}/HMC-S composite cathode exhibits a high initial capacity of 945 mA h g^{-1} with a high retained capacity of 526 mA h g^{-1} and a coulombic efficiency of nearly 100% after 500 cycles. The present work sheds light on the design of novel functional electrodes for next-generation electrochemical cells based on a simple yet effective vacancy engineering strategy.

Received 15th February 2019
Accepted 15th April 2019

DOI: 10.1039/c9ta01722d

rsc.li/materials-a

Introduction

Compared to lithium-ion[1] and sodium-ion batteries,[2] lithium–sulfur (Li–S) batteries are very promising for large-scale energy storage due to their high theoretical energy density (2600 W h kg^{-1}), earth-abundance of sulfur and environmental friendliness.[3] However, the commercialization of Li–S technology has still been prevented by its poor cyclability arising from several critical challenges: (1) low active sulfur utilization and high polarization caused by low conductivity of the sulfur cathode and its discharge product (Li_2S_2/Li_2S); (2) low coulombic efficiency and fast capacity fading as well as increased erosion of the lithium anode stemming from the shuttling effect of soluble polysulfide intermediates; and (3) cathode disintegration during cycling induced by huge volume fluctuation of S during repeated charge/discharge.

Much effort has been devoted to mitigating the challenges of Li–S cells, including regulating the cathode composition/structure,[4] exploring functional binders[5,6] or separators,[7,8] and using smart interlayers.[9] Among these, designing functional cathode hosts for high S-loading has been a general and effective approach. Various carbon nanomaterials, such as micro/mesoporous carbon,[10,11] hollow carbon,[12] carbon nanotubes (CNTs),[13] graphene and their hybrids,[14] have been widely used to block the shuttling of polysulfides and improve the electronic conductivity of sulfur. Nonetheless, the van der Waals interactions between carbon and polysulfides remain weak for sufficient suppression of their dissolution and shuttling, causing gradual capacity fading.[15] To overcome this, polar materials with stronger chemical interactions with polysulfides, such as metal oxides/hydroxides,[16–18] sulfides,[19,20] selenides,[21] nitrides,[22–25] phosphides,[26] and their composites[27,28] have been investigated to enhance the anchoring capability towards polysulfide intermediates. Particularly, the Lee group recently reported two-dimensional layer-structured MoS_2 nanoflakes with sulfur vacancies as a cathode host material for Li–S batteries with high affinity to polar polysulfides and superior catalytic activity for polysulfide conversion as unravelled by symmetry cyclic voltammetry analyses.[29] However, the rate capability and long-term cyclability of such composite cathodes still need further improvement for practical applications.

[a]State Key Laboratory of Advanced Technology for Materials Synthesis and Processing, Wuhan University of Technology, Wuhan 430070, China. E-mail: hongenwang@whut.edu.cn

[b]Center of Super Diamond & Advanced Films (COSDAF), Department of Materials Science and Engineering, City University of Hong Kong, HKSAR, China. E-mail: apwjzh@cityu.edu.hk

[c]Department of Materials Science and Technology, Southern University of Science and Technology, Shenzhen 518055, China

[d]Institute of Chemical Materials, China Academy of Engineering Physics, Mianyang 621900, China

[e]Department of Materials Science and Engineering, University of Washington, Seattle, WA 98195, USA. E-mail: gzcao@u.washington.edu

† Electronic supplementary information (ESI) available: Experimental, additional SEM/TEM/Raman/XPS/XRD/DFT, N_2 adsorption isotherms, TGA, and more battery testing data. See DOI: 10.1039/c9ta01722d

Uniformly blending MoS_2 with conductive, lightweight substances (*e.g.* graphene and CNTs) has been a common and effective strategy to enhance the electrical conduction of the resulting electrodes.[30] However, it is still challenging to develop homogeneous MoS_2-based hybrids. In this work, we report a novel composite host composed of hollow mesoporous carbon (HMC) spheres coupled with defective MoS_2 (MoS_{2-x}/HMC) for Li–S batteries with enhanced performance. The few-layered, sulfur-deficient MoS_2 nanosheets (MoS_{2-x}) have been mainly grown on the inner walls of the HMC spheres by interfacial C–S bonding. Such a unique structure endows the composite host with several unique structural advantages for use in Li–S cells: (1) compared to recent work,[29] few-layered MoS_2 nanosheets with enriched sulfur vacancies ($V_S^{\cdot\cdot}$) can afford more active sites for enhanced chemical adsorption of polysulfides and to propel their redox conversion, as proved by systematic characterization; more importantly, the interactions of sulfur-deficient MoS_2 and polysulfides and Li^+ diffusion on MoS_2 basal planes were better understood with detailed first-principles density functional theory (DFT) calculations; (2) the hollow mesoporous carbon (HMC) spheres with a high specific surface area effectively enhance the electron transport of the composite host and improve the charge transfer from carbon to MoS_{2-x} due to strong interfacial coupling with C–S bonds; (3) HMC with large inner voids also facilitates electrolyte permeation and accommodates the active material sulfur as well as effectively buffers its volume fluctuation during long-term cycling. The synergy of these merits enables the resultant MoS_{2-x}/HMC-S cathode to possess superior electrochemical performance in terms of a high capacity (1157 mA h g^{-1} at 0.2C), good rate capability (563 mA h g^{-1} at 5C), and stable cycling properties (526 mA h g^{-1} over 500 cycles at 1C).

Results and discussion

Structural characterization

The fabrication of the MoS_{2-x}/HMC composite is shown in Scheme 1. First, the hollow mesoporous carbon (HMC) precursor was prepared by a co-polymerization process with *in situ* hydrolysed SiO_2 colloids as templates, followed by carbonization. The resultant carbon product consists of uniform hollow spheres with diameters of 200–500 nm, uniform wall thickness (~60 nm) and straight mesoporous channels, as revealed by scanning and transmission electron microscopy (SEM/TEM) images (Fig. S1a and b, ESI†). The formation of hollow and mesoporous nanostructures can be ascribed to the removal of colloidal SiO_2 nanoparticles. Next, MoS_2 nanosheets were hydrothermally grown inside HMC, followed by annealing in H_2/Ar (5%/95%). In this process, HMC facilitates heterogeneous nucleation and growth of homogeneous, ultrathin MoS_2 sheets primarily on the inner surface of the HMC spheres. Then, annealing in H_2 creates sulfur vacancies ($V_S^{\cdot\cdot}$) in MoS_2.

From SEM images (Fig. S1c and d†), only a few MoS_2 nanosheets were anchored on the outer surface of the HMC spheres, hinting the preferential growth of MoS_2 inside HMC, as further validated by the TEM image (Fig. 1a). The as-synthesized MoS_2 nanosheets possess an ultrathin thickness of ~6 nm, corresponding to less than 10 sandwich S–Mo–S layers (Fig. S2a†). The interplanar distance between the lattice fringes is measured to be ~0.65 nm (Fig. S2b†), which can be indexed to the (002) planes with some dislocations (Fig. S2c†) of hexagonal MoS_2 crystals.[31] Note that the pore volume has been reduced from 1.31 cm^3 g^{-1} for HMC to 0.39 cm^3 g^{-1} for the MoS_2/HMC composite (Fig. S3 and Table S1†) due to the growth of MoS_2 inside the hollow carbon spheres as well as the larger molecular weight of MoS_2 relative to carbon. Nevertheless, the well-dispersed ultrathin MoS_2 nanosheets endow the composite with a relatively high surface area of 146.6 m^2 g^{-1} with a MoS_2 content of 75.2 wt% (Fig. S4†). The hexagonal symmetry has been further confirmed by the two-dimensional lattice image in high-resolution TEM (HRTEM, Fig. 1b) combined with the fast Fourier transform (FFT) pattern (inset), showing the resolved (10−1) and (012) crystal planes. The composition and element distribution of the as-prepared product were further characterized by high angle annular dark field STEM (HAADF-STEM) fitted with energy-dispersive X-ray (EDX) maps (Fig. 1c–f). The EDX map result verifies the confined growth of ultrathin MoS_2 sheets mainly inside the HMC spheres.

The crystal structures were further investigated by X-ray diffraction (XRD) and Raman spectroscopy. In Fig. 2a, the absence of any diffraction peaks reveals the amorphous feature of the HMC product. For MoS_2/HMC, all diffraction peaks can

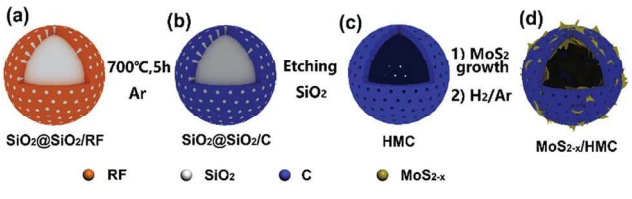

Scheme 1 Fabrication of sulfur-deficient MoS_2 grown on hollow mesoporous carbon spheres. (a) Synthesis of the carbon precursor with SiO_2 colloids as the template, (b) fabrication of carbon with a SiO_2 template, (c) synthesis of hollow mesoporous carbon (HMC) after removing SiO_2 using NaOH etching, and (d) growth of ultrathin MoS_2 with $V_S^{\cdot\cdot}$ on the HMC surface. RF: resorcinol formaldehyde resin.

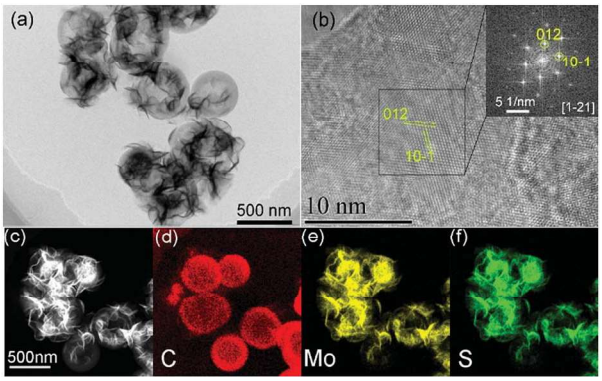

Fig. 1 (a) TEM and (b) HRTEM images and the FFT pattern (inset), and (c) dark-field STEM image and corresponding EDX maps of C (d), Mo (e) and S (f) elements in the MoS_{2-x}/HMC product.

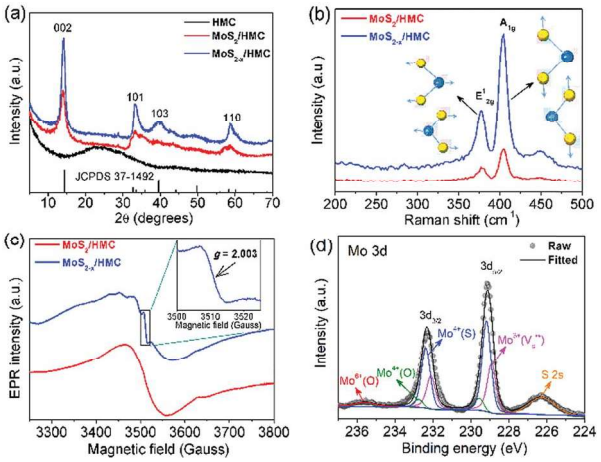

Fig. 2 (a) XRD, (b) Raman, (c) EPR and (d) Mo 3d XPS spectra of MoS_{2-x}/HMC.

be indexed to 2H-type MoS_2 with hexagonal symmetry (JCPDS card no. 37-1492).[32] After annealing in H_2/Ar, the as-obtained MoS_{2-x}/HMC retains the hexagonal structure with higher crystallinity. The average crystallite size along the *z*-axis was calculated to be *ca.* 7.2 nm based on the full width at half maximum (FWHM) value of the (002) diffraction peak from the Scherrer equation, which is similar to the nanosheet thickness (~6 nm) measured by TEM characterization (Fig. S2a†). In addition, it is noted that the relative diffraction peak intensity of (101) and (110) is much stronger than that from the standard JCPDS card, which can be caused by the ultrathin nanosheet structure of the resultant MoS_2 products. In Raman spectra (Fig. 2b), the two bands at 378 cm^{-1} and 405 cm^{-1} in the two samples correspond to the A_{1g} and E^1_{2g} modes of the 2H phase with a trigonal prismatic structure.[33] The absence of a Raman signal at ~200 and 225 cm^{-1} unravels that no 1T (1T′) phase coexists with a (distorted) octahedral structure.[34] In addition, the two bands located at 1334 and 1593 cm^{-1} can be ascribed to the D and G bands of amorphous carbon from the HMC spheres (Fig. S5a†).[35] The intensity ratio of the G *versus* D band (I_G/I_D) is slightly larger than unity, suggesting a high graphitization degree and superior electron transport capability for the electrochemical reaction.

Electron paramagnetic resonance (EPR) spectra reveal more defect information of the resultant MoS_2 products. From Fig. 2c, a broad hump can be observed with a *g*-factor of 2.002, representing the existence of Mo^{3+} with an unpaired electron configuration of $4d^3$.[36] In addition, the presence of sulfur vacancies ($V_S^{\cdot\cdot}$) with a *g*-factor of 2.003 can be exclusively observed in MoS_{2-x}/HMC as highlighted by a rectangular region and amplified in the inset for clarity.[37,38] The elemental composition and surface electronic states were probed by X-ray photoelectron spectroscopy (XPS) analysis. The deconvolution of the C 1s spectrum (Fig. S5b†) reveals four peaks at 284.3 eV (C–C), 285.6 eV (C–S), 286.9 eV (C–O) and 288.5 eV (C=O), respectively.[39] Specifically, the formation of C–S bonding at the HMC and MoS_2 interface is crucial for enhanced electronic coupling, which can improve the structural stability of the composite and electron transfer from carbon to MoS_2. In the Mo 3d XPS spectrum (Fig. 2d), two major bands at 229.2 eV and 232.4 eV can be assigned to Mo $3d_{5/2}$ and Mo $3d_{3/2}$ of Mo^{4+} in MoS_2. Another two bands at 228.9 eV and 232.1 eV can be assigned to the Mo^{3+} signals.[34] In addition, two minor bands at 229.6 eV and 232.8 eV can be attributed to the O–Mo^{4+} bonds formed by substitution of minor S in the basal plane with O.[40] A minor band at 226.3 eV represents the S 2s signal.[31] Another minor band at ~235.6 eV corresponds to Mo^{6+} due to surface oxidation. From the areal ratio, the concentration of Mo^{3+} on the surface is calculated to be *ca.* 32%. If the formation of one $V_S^{\cdot\cdot}$ is accompanied by the production of two Mo^{3+} simultaneously, the concentration of $V_S^{\cdot\cdot}$ on the surface can be roughly estimated as *ca.* 16%.

DFT calculations of the influence of $V_S^{\cdot\cdot}$ on the chemical affinity of MoS_2 to polysulfides

Next, we used DFT calculations to investigate the influence of $V_S^{\cdot\cdot}$ on electronic structures of MoS_2 crystals. Fig. 3a and c show the optimized geometry configuration of the pristine monolayer $p(3 \times 3 \times 1)$ MoS_2 supercell composed of sandwich S–Mo–S layers and the corresponding partial density of states (PDOS). The calculation result suggests that the MoS_2 crystal is a semiconductor with a calculated bandgap (E_g) of ~1.8 eV, which is in consistent with recent literature.[40] PDOS analysis indicates that the valence band (VB) and conduction band (CB) are mainly composed of the S 2p orbital and the Mo 3d orbital, respectively. Fig. 3b and d show the optimized geometry structure of the MoS_2 supercell with one $V_S^{\cdot\cdot}$ on the basal plane and the corresponding PDOS. Compared to Fig. 3b, one gap state (indicated by a black arrow) is found in the PDOS plot of defective MoS_2, leading to decreased E_g and enhanced electronic conductivity.[31]

Next, the adsorption of polysulfides on MoS_2 was simulated using Li_2S_4 as a model polysulfide molecule. On the surface of pristine MoS_2, Li_2S_4 tends to be adsorbed on the basal plane *via*

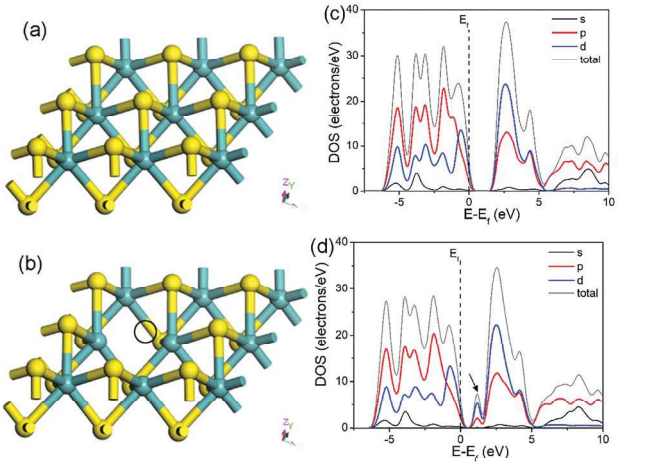

Fig. 3 Optimized geometry structures of the monolayer MoS_2 $3 \times 3 \times 1$ supercell (a) and MoS_2 with $V_S^{\cdot\cdot}$; (c and d) corresponding density of states (DOS) of pristine MoS_2 (c) and MoS_2 with $V_S^{\cdot\cdot}$ (d). The cyan and yellow spheres represent Mo and S atoms, respectively. The black circle in (b) depicts $V_S^{\cdot\cdot}$.

formation of two Li···S bonds (with bond lengths of 2.434 Å and 2.457 Å, respectively) between Li_2S_4 and MoS_2 slabs (Fig. S6a and b†). The calculated adsorption energy (E_{ads}) is −1.84 eV, which is much larger than that of WS_2 (0.51–1.4 eV) and graphitic carbon (0.1–0.51 eV),[20] suggesting the chemisorption of polysulfide by MoS_2. In comparison, Li_2S_4 has two preferential positions on the MoS_2 surface (Fig. 4a–c). In the first one, the two Li atoms in Li_2S_4 tend to face downward to the MoS_2 basal plane and form four Li···S bonds at the interface, albeit with slightly elongated bond lengths (2.594–2.872 Å). The calculated E_{ads} is −1.85 eV, similar to that of the pristine MoS_2. In another configuration, one S atom in Li_2S_4 can be trapped at the affinity of $V_S^{\cdot\cdot}$ with a much higher E_{ads} of −4.12 eV. The calculation results unravel that MoS_2 with $V_S^{\cdot\cdot}$ can strongly bind polysulfides by formation of either Li···S bonds or S···Mo bonds at the Li_2S_4/MoS_2 interface. The high affinity of MoS_{2-x} to polysulfides has been further verified by a simple visual adsorption experiment whereas the colour of the Li_2S_6 solution quickly fades after adding MoS_{2-x}/HMC (Fig. 4d). In addition, the trapped S atom has a significantly elongated bond length with the adjacent S and Li atoms (3.267 Å and 2.97 Å, respectively), suggesting that the original adsorbed Li_2S_4 molecule is unstable and tends to further decompose into lower-order polysulfides. Recent studies reveal that the decomposition of higher-order polysulfides on a conductive host is beneficial for fast reaction kinetics.[41] Herein, we speculate that the conversion kinetics of polysulfides on the MoS_{2-x}/HMC host can be accelerated considering its superior electronic conductivity enabled by the presence of $V_S^{\cdot\cdot}$ and electron coupling of MoS_2 with HMC.

To further study the redox kinetics information and the effect of $V_S^{\cdot\cdot}$ on Li transport, we further modelled Li diffusion on the pristine MoS_2 surface (Fig. S6c and d†) and MoS_{2-x} (Fig. 5a and b), respectively. The calculated energy barriers for Li ion diffusion are 0.47 eV for MoS_2 and 0.54 eV for MoS_{2-x} (Fig. 5c), respectively, which are comparable to those of the Sb_2S_3 nanosheets host (~0.31 eV)[42] and much smaller than those of SnO_2 (~1.0 eV) and 1T-MoS_2 (~0.8 eV).[43] This result indicates that Li can move freely on both the pristine MoS_2 surface and $V_S^{\cdot\cdot}$-containing surface, contributing to high ionic conductivity. Thus, MoS_{2-x}/HMC can propel fast polysulfide conversion during charge/discharge combining both high electronic/ionic transport capabilities. The enhanced kinetics for polysulfide conversion on the MoS_{2-x} surface have been further validated by cyclic voltammetry (CV) measurements with symmetry MoS_2/C electrodes (Fig. 5d). Compared to MoS_2/HMC, the MoS_{2-x}/HMC electrode exhibits faster redox kinetics with lower onset potentials and larger current responses during cathodic/anodic processes, hinting that the transformation of polysulfides to either Li_2S (during discharge) or S (during recharge) proceeds more easily.

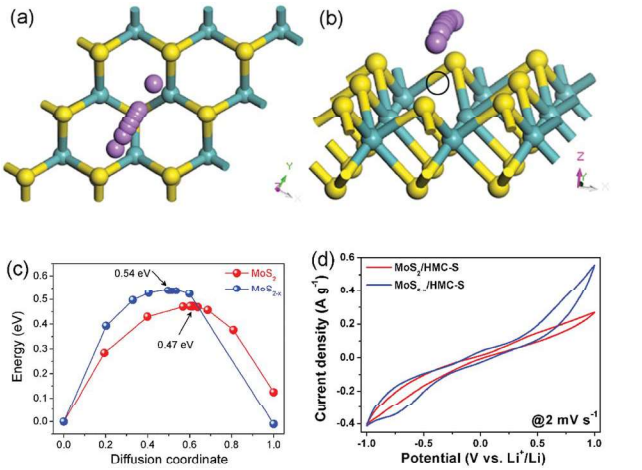

Fig. 5 (a and b) Li ion diffusion pathway on MoS_2 with $V_S^{\cdot\cdot}$, (c) energy profiles of Li ion diffusion on pristine MoS_2 and MoS_2 with $V_S^{\cdot\cdot}$, and (d) CV curves of Li-polysulfide cells with symmetric MoS_2/HMC or MoS_{2-x}/HMC electrodes. Cyan, yellow, and pink balls represent Mo, S, and Li atoms, respectively. The black circle in (b) depicts $V_S^{\cdot\cdot}$.

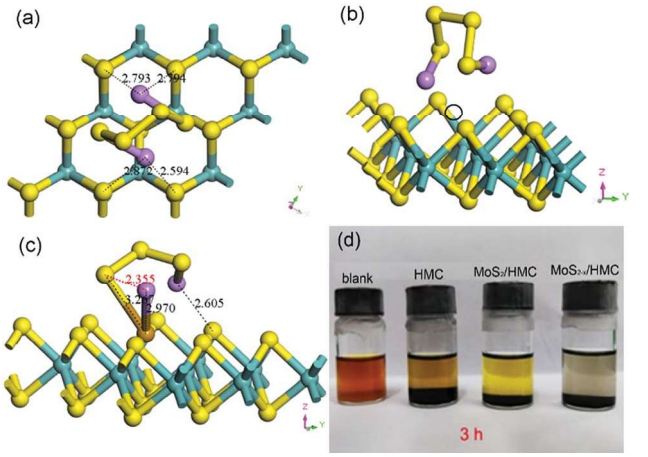

Fig. 4 (a–c) Optimized adsorption configurations of Li_2S_4 on MoS_2 with $V_S^{\cdot\cdot}$, and (d) visual adsorption experiments on a blank Li_2S_6 electrolyte and Li_2S_6 electrolytes after adding HMC, MoS_2/HMC and MoS_{2-x}/HMC, respectively.

Electrochemical performance evaluation of the MoS_2/C–S composite

The structural characterization and theoretical calculations suggest that the resultant MoS_{2-x}/HMC is promising for application in Li–S batteries. Next, as a proof-of-concept the composite was used as a sulfur host to assemble the Li–S cells. To prepare the composite cathodes, sulfur species were respectively loaded into MoS_{2-x}/HMC, MoS_2/HMC, and HMC by a conventional melt-diffusion method. The resultant composite was characterized by XRD, TGA, and SEM as shown in Fig. S7 and S8,† proving that sulfur has been uniformly incorporated into the host. Note that the use of SEM instead of TEM in Fig. S8† to check sulfur filling is mainly based on the fact that sulfur is unstable and prone to sublimation under intensive e-beam irradiation in a high vacuum. In addition, the sulfur loading (~60 wt% shown in Fig. S7a†) is not high compared to that mentioned in some latest literature studies (70–80 wt%) but a similar loading level is also routinely use in recent literature.[18] The slightly low sulfur loading is mainly limited by the

not very high pore volume of the resultant MoS_2/HMC composites, and further work is ongoing to further improve the sulfur loading on such cathode hosts.

Electrochemical performance of the cathodes was investigated using cyclic voltammetry (CV), galvanostatic charge/discharge (GCD) and electrochemical impedance spectroscopy (EIS) tests. Initial CV curves of the MoS_{2-x}/HMC-S cathode recorded at 0.2 mV s^{-1} (Fig. S9a†) reveal two reduction peaks at ~2.3 V and 2.0 V in the cathodic process, representing the stepwise reduction of S into long-chain polysulfides (Li_2S_x, $3 < x \leq 8$) and then to Li_2S_2/Li_2S during discharge.[44] In the anodic process, one oxidation peak noted at ~2.45 V corresponds to the re-oxidation of short-chain polysulfides to long-chain polysulfides and finally to elemental S. The reduction peaks shift positively and oxidation peak shifts negatively in the 2nd scan, suggesting improved electrode kinetics, while the rough superposition of the 3rd and 2nd curves signifies good electrode reversibility. The GCD curves of the MoS_{2-x}/HMC-S cathode (Fig. S9b†) present two potential plateaus at ~2.3 V and 2.1 V during discharge, and one long potential plateau at ~2.3 V during charge, in good agreement with the CV result (Fig. S9a†). The MoS_{2-x}/HMC-S cathode manifests a high initial discharge and charge capacity of 1186 and 1153 mA h g^{-1}, with a high coulombic efficiency (CE) of 97.2%.

CV profiles of the three cathodes (Fig. 6a) reveal that MoS_{2-x}/HMC-S exhibits the smallest polarization and the largest current response, demonstrating its fastest reaction kinetics with highest S utilization. Similar conclusions can also be drawn from the GCD curves of the three electrodes (Fig. 6b), whereas the MoS_{2-x}/HMC-S cathode exhibits the highest initial discharge/charge capacity and the lowest polarization ($\Delta V1$ = 190 mV), much smaller than that of MoS_2/HMC-S ($\Delta V2$ = 212 mV) and HMC-S ($\Delta V3$ = 250 mV). The higher capacity and smaller polarization of MoS_{2-x}/HMC can be mainly ascribed to the synergistic enhancement of electronic/ionic transport properties of $V_S^{\cdot\cdot}$-enriched MoS_2 as discussed above. The Li^+ diffusion coefficient (D) was further determined by CV sweep at varying scan rates (Fig. S10a and b†) using the Randles–Sevcik equation: $i_p = (2.69 \times 10^5)n^{3/2}AD^{1/2}Cv^{1/2}$, where n represents the number of electrons in the redox process ($n - 2$), A is the electrode area, C is the concentration of Li^+ (here 1 mM), and v is the scan rate. According to the above equation, the plot of peak current (i_p) *versus* square root of the scan rate ($v^{1/2}$) is shown in Fig. S10c,† and the diffusion coefficient (D) is calculated to be 1.27×10^{-8} cm^2 s^{-1} for the cell with MoS_{2-x}/HMC-S, which is larger than that for the cell with MoS_2/HMC-S (4.71×10^{-9} cm^2 s^{-1}). The calculated D value is also comparable to the results of recent literature.[45] In addition, MoS_{2-x}/HMC exhibits superior cycling and rate capability. From Fig. 6c, the MoS_{2-x}/HMC-S cathode retains a reversible capacity of 754 mA h g^{-1} over 100 cycles at 0.2C with a high retention rate of 70%, better than that of MoS_2/HMC-S (58.5%) and HMC-S (51.1%) counterparts. Moreover, GCD curves of the MoS_{2-x}/HMC-S cathode at 0.2C show well-defined potential profiles with low polarization and slow capacity degradation during the 5th, 10th, 20th, 50th and 100th cycles (Fig. S9c†). From the rate property test in Fig. 6d, the MoS_{2-x}/HMC-S cathode delivers stable and high rate capacities of 1020, 876, 800, 730 and 528.3 mA h g^{-1} at increasing current rates of 0.2, 0.5, 1, 2 and 5C, respectively. Accordingly, its GCD curves (Fig. S9d†) display low polarization and well-defined potential plateaus with increasing charge/discharge rates, validating good kinetics. After switching the current rate back to 0.2C again, it can restore a reversible capacity of 920 mA h g^{-1}. In contrast, both MoS_2/HMC-S and HMC-S electrodes deliver inferior rate properties. When tested at 1C for 500 cycles (Fig. 6e), the MoS_{2-x}/HMC-S cathode manifests a capacity of 530 mA h g^{-1}, higher than that of MoS_2/HMC-S (426 mA h g^{-1}) and HMC-S (335 mA h g^{-1}). Apparently, the HMC-S cathode exhibits the best cyclability. Careful inspection reveals that such a misconception can be possibly caused by the very low capacity of the HMC-S cathode in the beginning, mainly stemming from the severe shuttling effect due to the weak interaction between nonpolar carbon and polar polysulfides. Even at 3C rate (Fig. S9e†), the MoS_{2-x}/HMC-S composite cathode can sustain a capacity of 445 mA h g^{-1} over 300 cycles, better than that of MoS_2/HMC-S (284 mA h g^{-1}).

The enhanced electrode kinetics were further confirmed by in-depth EIS analysis of the Li–S cells with the three kinds of cathodes, respectively (Fig. S11†). All three Nyquist plots can be fitted with an equivalent electric circuit model shown in the inset. After fitting, all the three cells have similar series resistance (R_s) values of 1.4–1.7 Ω. However, the MoS_{2-x}/HMC cathode exhibits the smallest charge transfer resistance (R_{ct}, 59.6 Ω), lower than that of MoS_2/HMC-S (65.9 Ω) and HMC-S (71.8 Ω). The decreased R_{ct} signifies fast redox kinetics of the

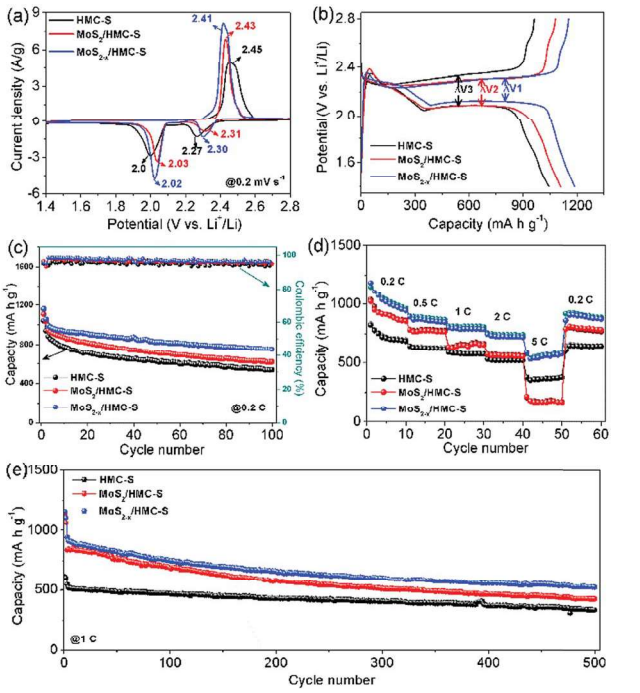

Fig. 6 Electrochemical performance of the Li–S cells using MoS_{2-x}/HMC-S, MoS_2/HMC-S and HMC-S cathodes, respectively. (a) CV curves at 0.2 mV s^{-1}, (b) GCD curves at 0.2C rate, (c) cycling performance at 0.2C rate, (d) rate capability, and (e) long-term cycling properties at 1C rate

of Li–S cell with MoS_{2-x}/HMC-S during charging/discharging, which supports its higher capacity and better rate properties (Fig. 6). The boosted kinetics mainly arise from the simultaneously enhanced electron/Li-ion transport capability on the sulfur-deficient MoS_2 surface as suggested by the DFT simulations (Fig. 3 and 5).

The outstanding electrochemical performances of the MoS_{2-x}/HMC-S electrode can be mainly ascribed to the following unique structural merits: (1) $V_S^{\cdot\cdot}$ effectively enhances the chemical trapping capability of MoS_2 to immobilize polysulfides and reduce their shuttling; (2) the high electronic/ionic transport capability in $V_S^{\cdot\cdot}$-enriched MoS_2 coupled with HMC enhances the polysulfides' conversion kinetics and enables superior rate capability; and (3) the high specific surface area and pore volume of HMC and ultrathin MoS_2 nanosheets can accommodate a large amount of S, alleviate its volume expansion during discharge, and reduce the electron/ion diffusion paths. The synergistic interaction of the above features endows the composite with outstanding electrochemical properties in Li–S batteries, which outperforms several recently reported Li–S cells with diverse cathode hosts, as summarized in Table S2.†

Conclusions

Sulfur-deficient MoS_2 ultrathin nanosheets have been grown inside hollow mesoporous carbon spheres. The resultant composite serves as an ideal functional cathode host for Li–S batteries with superior electrochemical properties. The enormous $V_S^{\cdot\cdot}$ acts as both active site for polysulfide immobilization and activation site for catalyzing polysulfide conversion, as revealed by combined experimental and first principles DFT simulation methods. The presented strategy based on vacancy defect engineering can pave the way for rational design and exploration of a wide array of novel multifunctional electrode materials for high-performance lithium–sulfur batteries and beyond.

Conflicts of interest

There are no conflicts to declare.

Acknowledgements

This work is financially supported by the National Natural Science Foundation of China (51672230), CityU Applied Research Grant (ARG 9667159), and in part by the National Science Foundation (No. 1803256). H.-E. Wang acknowledges the Hubei Provincial Department of Education for the "Chutian Scholar" program.

Notes and references

1 (*a*) L. Zhao, H. H. Wu, C. Yang, Q. Zhang, G. Zhong, Z. Zheng, H. Chen, J. Wang, K. He, B. Wang, T. Zhu, X. C. Zeng, M. Liu and M. S. Wang, *ACS Nano*, 2018, **12**, 12597–12611; (*b*) Q. Zhang, H. Chen, L. Luo, B. Zhao, H. Luo, X. Han, J. Wang, C. Wang, Y. Yang, T. Zhu and M. Liu, *Energy Environ. Sci.*, 2018, **11**, 669–681; (*c*) Z. Zheng, H. H. Wu, H. Chen, Y. Cheng, Q. Zhang, Q. Xie, L. Wang, K. Zhang, M. S. Wang, D. L. Peng and X. C. Zeng, *Nanoscale*, 2018, **10**, 22203; (*d*) Y. Cai, H. E. Wang, X. Zhao, F. Huang, C. Wang, Z. Deng, Y. Li, G. Cao and B. L. Su, *ACS Appl. Mater. Interfaces*, 2017, **9**, 10652–10663; (*e*) W. An, B. Gao, S. Mei, B. Xiang, J. Fu, L. Wang, Q. Zhang, P. K. Chu and K. Huo, *Nat. Commun.*, 2019, **10**, 1447.

2 X. Zhao, W. Cai, Y. Yang, X. Song, Z. Neale, H. E. Wang, J. Sui and G. Cao, *Nano Energy*, 2018, **47**, 224–234.

3 (*a*) A. Manthiram, Y. Fu, S.-H. Chung, C. Zu and Y.-S. Su, *Chem. Rev.*, 2014, **114**, 11751–11787; (*b*) G. R. Li, S. Wang, Y. N. Zhang, M. Li, Z. W. Chen and J. Lu, *Adv. Mater.*, 2018, **30**, 1705590; (*c*) R. P. Fang, S. Y. Zhao, Z. H. Sun, W. Wang, H. M. Cheng and F. Li, *Adv. Mater.*, 2017, **29**, 1606823.

4 X. Liu, J. Q. Huang, Q. Zhang and L. Q. Mai, *Adv. Mater.*, 2017, **29**, 1601759.

5 W. Chen, T. Qian, J. Xiong, N. Xu, X. J. Liu, J. Liu, J. Q. Zhou, X. W. Shen, T. Z. Yang, Y. Chen and C. L. Yan, *Adv. Mater.*, 2017, **29**, 1605160.

6 J. Liu, Q. Zhang and Y.-K. Sun, *J. Power Sources*, 2018, **396**, 19–32.

7 M. S. Kim, L. Ma, S. Choudhury and L. A. Archer, *Adv. Mater. Interfaces*, 2016, **3**, 1600450.

8 J. R. He, Y. F. Chen and A. Manthiram, *Energy Environ. Sci.*, 2018, **11**, 2560–2568.

9 A. Manthiram, Y. Z. Fu and Y. S. Su, *Acc. Chem. Res.*, 2013, **46**, 1125–1134.

10 P. Wu, L. H. Chen, S. S. Xiao, S. Yu, Z. Wang, Y. Li and B. L. Su, *Nanoscale*, 2018, **10**, 11861–11868.

11 M. Chen, W. Wang, X. Liang, S. Gong, J. Liu, Q. Wang, S. J. Guo and H. Yang, *Adv. Energy Mater.*, 2018, **8**, 1800171.

12 F. Pei, L. L. Lin, D. H. Ou, Z. M. Zheng, S. G. Mo, X. L. Fang and N. F. Zheng, *Nat. Commun.*, 2017, **8**, 482.

13 M. Yan, H. Chen, Y. Yu, H. Zhao, C. F. Li, Z. Y. Hu, P. Wu, L. H. Chen, H. E. Wang, D. L. Peng, H. X. Gao, T. Hasan, Y. Li and B. L. Su, *Adv. Energy Mater.*, 2018, **8**, 1801066.

14 Z. Zhang, L. L. Kong, S. Liu, G. R. Li and X. P. Gao, *Adv. Energy Mater.*, 2017, **7**, 1602543.

15 X. Ji, K. T. Lee and L. F. Nazar, *Nat. Mater.*, 2009, **8**, 500–506.

16 (*a*) Q. Pang, D. Kundu, M. Cuisinier and L. F. Nazar, *Nat. Commun.*, 2014, **5**, 4759; (*b*) X. Liang, C. Hart, Q. Pang, A. Garsuch, T. Weiss and L. F. Nazar, *Nat. Commun.*, 2015, **6**, 5682.

17 J. T. Zhang, Z. Li, Y. Chen, S. Y. Gao and X. W. Lou, *Angew. Chem., Int. Ed.*, 2018, **57**, 10944–10948.

18 H. E. Wang, K. Yin, N. Qin, X. Zhao, F. J. Xia, Z. Y. Hu, G. Guo, G. Cao and W. Zhang, *J. Mater. Chem. A*, 2019, **7**, 10346–10353.

19 (*a*) G. M. Zhou, H. Z. Tian, Y. Jin, X. Y. Tao, B. F. Liu, R. F. Zhang, Z. W. Seh, D. Zhuo, Y. Y. Liu, J. Sun, J. Zhao, C. X. Zu, D. S. Wu, Q. F. Zhang and Y. Cui, *Proc. Natl. Acad. Sci. U. S. A.*, 2017, **114**, 840–845; (*b*) L. Hu, C. Dai, J. M. Lim, Y. Chen, X. Lian, M. Wang, Y. Li, P. Xiao, G. Henkelman and M. Xu, *Chem. Sci.*, 2018, **9**, 666–675.

20 (*a*) S. Z. Huang, Y. Wang, J. P. Hu, Y. V. Lim, D. Z. Kong, Y. Zheng, M. Ding, M. E. Pam and H. Y. Yang, *ACS Nano*,

2018, **12**, 9504–9512; (*b*) C. Dai, L. Hu, X. Li, Q. Xu, R. Wang, H. Liu, H. Chen, S. J. Bao, Y. M. Chen, G. Henkelman, C. M. Li and M. Xu, *Nano Energy*, 2018, **53**, 354–361.

21 C.-Y. Fan, Y.-P. Zheng, X.-H. Zhang, Y.-H. Shi, S.-Y. Liu, H.-C. Wang, X.-L. Wu, H.-Z. Sun and J.-P. Zhang, *Adv. Energy Mater.*, 2018, **8**, 1703638.

22 Z. M. Cui, C. X. Zu, W. D. Zhou, A. Manthiram and J. B. Goodenough, *Adv. Mater.*, 2016, **28**, 6926.

23 Z. X. Hao, L. X. Yuan, C. J. Chen, J. W. Xiang, Y. Y. Li, Z. M. Huang, P. Hu and Y. H. Huang, *J. Mater. Chem. A*, 2016, **4**, 17711–17717.

24 L. Zhang, X. Chen, F. Wan, Z. Niu, Y. Wang, Q. Zhang and J. Chen, *ACS Nano*, 2018, **12**, 9578–9586.

25 L. B. Ma, H. Yuan, W. J. Zhang, G. Y. Zhu, Y. R. Wang, Y. Hu, P. Y. Zhao, R. P. Chen, T. Chen, J. Liu, Z. Hu and Z. Jin, *Nano Lett.*, 2017, **17**, 7839–7846.

26 S. Z. Huang, Y. V. Lim, X. M. Zhang, Y. Wang, Y. Zheng, D. Z. Kong, M. Ding, S. Y. A. Yang and H. Y. Yang, *Nano Energy*, 2018, **51**, 340–348.

27 (*a*) X. Li, G. Guo, N. Qin, Z. Deng, Z. Lu, D. Shen, X. Zhao, Y. Li, B.-L. Su and H.-E. Wang, *Nanoscale*, 2018, **10**, 15505–15512; (*b*) H.-E. Wang, K. Yin, X. Zhao, N. Qin, Y. Li, Z. Deng, L. Zheng, B.-L. Su and Z. Lu, *Chem. Commun.*, 2018, **54**, 12250–12253.

28 L. Hu, C. Dai, H. Liu, Y. Li, B. Shen, Y. Chen, S. J. Bao and M. Xu, *Adv. Energy Mater.*, 2018, **8**, 1800709.

29 H. B. Lin, L. Q. Yang, X. Jiang, G. C. Li, T. R. Zhang, Q. F. Yao, G. W. Zheng and J. Y. Lee, *Energy Environ. Sci.*, 2017, **10**, 1476–1486.

30 Y. You, Y. Ye, M. Wei, W. Sun, Q. Tang, J. Zhang, X. Chen, H. Li and J. Xu, *Chem. Eng. J.*, 2019, **355**, 671–678.

31 J. F. Xie, J. J. Zhang, S. Li, F. Grote, X. D. Zhang, H. Zhang, R. X. Wang, Y. Lei, B. C. Pan and Y. Xie, *J. Am. Chem. Soc.*, 2013, **135**, 17881–17888.

32 J. F. Xie, H. Zhang, S. Li, R. X. Wang, X. Sun, M. Zhou, J. F. Zhou, X. W. Lou and Y. Xie, *Adv. Mater.*, 2013, **25**, 5807.

33 X. Zhang, R. Zhao, Q. Wu, W. Li, C. Shen, L. Ni, H. Yan, G. Diao and M. Chen, *ACS Nano*, 2017, **11**, 8429–8436.

34 X. J. Zhu, D. Li, X. G. Liang and W. D. Lu, *Nat. Mater.*, 2019, **18**, 141–148.

35 T. C. Fitzgibbons, M. Guthrie, E. S. Xu, V. H. Crespi, S. K. Davidowski, G. D. Cody, N. Alem and J. V. Badding, *Nat. Mater.*, 2015, **14**, 43–47.

36 C. J. Casewit and M. R. DuBois, *Inorg. Chem.*, 1986, **25**, 74–80.

37 Y. L. Zhang, Z. J. Mu, C. Yang, Z. K. Xu, S. Zhang, X. Y. Zhang, Y. J. Li, J. P. Lai, Z. H. Sun, Y. Yang, Y. G. Chao, C. J. Li, X. X. Ge, W. X. Yang and S. J. Guo, *Adv. Funct. Mater.*, 2018, **28**, 1707578.

38 M. K. Singh, P. Chettri, A. Tripathi, A. Tiwari, B. Mukherjee and R. K. Mandal, *Phys. Chem. Chem. Phys.*, 2018, **20**, 15817–15823.

39 H. E. Wang, X. Zhao, X. C. Li, Z. Y. Wang, C. F. Liu, Z. G. Lu, W. J. Zhang and G. Z. Cao, *J. Mater. Chem. A*, 2017, **5**, 25056–25063.

40 J. Pető, T. Ollár, P. Vancsó, Z. I. Popov, G. Z. Magda, G. Dobrik, C. Hwang, P. B. Sorokin and L. Tapasztó, *Nat. Chem.*, 2018, **10**, 1246–1251.

41 F. X. Wu, T. P. Pollard, E. B. Zhao, Y. R. Xiao, M. Olguin, O. Borodin and G. Yushin, *Energy Environ. Sci.*, 2018, **11**, 807–817.

42 S. S. Yao, J. Cui, J. Q. Huang, Z. H. Lu, Y. Deng, W. G. Chong, J. X. Wu, M. I. U. Haq, F. Ciucci and J. K. Kim, *Adv. Energy Mater.*, 2018, **8**, 1800710.

43 M. X. Wang, L. S. Fan, D. Tian, X. Wu, Y. Qiu, C. Y. Zhao, B. Guan, Y. Wang, N. Q. Zhang and K. N. Sun, *ACS Energy Lett.*, 2018, **3**, 1627–1633.

44 L. B. Ma, W. J. Zhang, L. Wang, Y. Hu, G. Y. Zhu, Y. R. Wang, R. P. Chen, T. Chen, Z. X. Tie, J. Liu and Z. Jin, *ACS Nano*, 2018, **12**, 4868–4876.

45 T. Zhou, Y. Zhao, G. Zhou, W. Lv, P. Sun, F. Kang, B. Li and Q. H. Yang, *Nano Energy*, 2017, **39**, 291–296.